View metadata, citation and similar papers at core.ac.uk
brought to you by CORE
provided by Diposit Digital de Documents de la UAB

Geologica Acta, Vol.8, N° 1, March 2010, 15-31
DOI: 10.1344/105.000001513
Available online at www.geologica-acta.com
geologica acta

# 2-D Niblett-Bostick magnetotelluric inversion

J. RODRÍGUEZ F.J. ESPARZA [*] and E. GÓMEZ-TREVIÑO

**CICESE/Ciencias de la Tierra**
Km 107 carr. Tijuana-Ensenada, Ensenada, B.C., 22860, México

* Corresponding author E-mail: fesparz@cicese.mx

## ABSTRACT

A simple and robust imaging technique for two-dimensional magnetotelluric interpretations has been developed following the well known Niblett-Bostick transformation for one-dimensional profiles.
The algorithm processes series and parallel magnetotelluric impedances and their analytical influence functions using a regularized Hopfield artificial neural network. The adaptive, weighted average approximation preserves part of the nonlinearity of the original problem, yet no initial model in the usual sense is required for the recovery of the model; rather, the built-in relationship between model and data automatically and concurrently considers many half spaces whose electrical conductivities vary according to the data. The use of series and parallel impedances, a self-contained pair of invariants of the impedance tensor, avoids the need to decide on best angles of rotation for identifying TE and TM modes. Field data from a given profile can thus be fed directly into the algorithm without much processing. The solutions offered by the regularized Hopfield neural network correspond to spatial averages computed through rectangular windows that can be chosen at will. Applications of the algorithm to simple synthetic models and to the standard COPROD2 data set illustrate the performance of the approximation.

*KEYWORDS* | **Niblett-Bostick inversion. Hopfield Neural Network. Magnetotelluric.**

## INTRODUCTION

Electromagnetic inverse problems in geophysics are nonlinear. Even relatively simple cases, like the one-dimensional (1-D) magnetotelluric (MT) problem, require special treatment to fully handle nonlinearities (e.g., Bailey, 1970; Weidelt, 1972; Parker, 1983). Methods based on linearization can be applied iteratively to handle the nonlinearity of the problem (e.g., Oldenburg, 1979; Smith and Booker, 1988). In practice, as well as not being linear, electromagnetic inverse problems are ill-posed and severely underconstrained. Sensible external constraints are usually imposed to construct realistic solutions that fit the data to a given degree. Most commonly, the norm of the solution or of its first or second derivative are minimized together with the misfit to the data. This technique, first developed for 1-D problems, can readily be applied in higher dimensions. Applications to the 2-D MT inverse problem include those of Rodi (1989), de Groot-Hedlin and Constable (1990), Smith and Booker (1988) and Rodi and Mackie (2001). Minimizing roughness avoids the appearance of sharp features in the solution models that are not strictly required by the data. That is, the resulting models are as smooth and even as the data permit.

It is also possible to obtain useful and somewhat more general information by slightly shifting the focus of attention; instead of looking for a single model that fits the data, one can ask for general properties of all possible models that fit the data. The method of Backus and Gilbert (e.g., Backus and Gilbert, 1968, 1970) allows for the computation of spatial averages by means of averaging functions constructed as linear combinations of the Fréchet derivatives of the data. The averaging functions are made to resemble box-car functions for the averages to have the usual intuitive meaning. The results are average models for given window sizes. The models are not intended to produce responses that fit the data. In fact, they seldom do better in this respect than models designed specifically for fitting purposes. It is perhaps for this reason that average models are not very popular among interpreters of field data who seem to prefer the assurance of a direct fit to the data.

Summarizing the above two paragraphs, we have on one side an optimization process of fitting data with external constraints, and on the other side, an optimization process of fitting Fréchet derivatives to box-car functions. Although the two processes are complementary, particularly for nonlinear problems, the latter is seldom applied, perhaps because it requires intensive computations, but most likely in view of the reason stated in the previous paragraph. In this paper, we present an approach that combines features from both methods. On one side, we keep the reassuring feature of constructing models whose responses optimize the fit to the data and, on the other, we maintain the concept of spatial averages. Spatial averages not only appeal to intuition, but when plotted against depth they resemble a profile of the property itself, filtered by the corresponding window. As shown in Gómez-Treviño (1996), a solution in terms of averages represents a robust alternative to the well known 1-D Niblett-Bostick transformation.

Between linearization and nonlinear methods, there are approximations simple enough to be handled analytically but that still keep some of the nonlinear features of the original problem. Such is the case of the Niblett-Bostick approximate integral equation (e.g., Niblett and Sayn-Wittgenstein, 1960; Bostick, 1977; Jones, 1983) which has inspired a number of generalizations. For instance: iteration of the corresponding exact equation (Esparza and Gómez-Treviño, 1996) and, still within the approximation, a solution of the non-uniqueness problem by direct computations of spatial averages (Gómez-Treviño, 1996). Other generalizations include the extension of the basic idea to 1-D inversion of controlled source electromagnetic data (e.g., Boerner and Holladay, 1990; Smith et al., 1994; Christensen, 1997).

The 1-D Niblett-Bostick approximation has the following basic features that are worthwhile exploiting in 2-D: a) it captures the basic physics in a simple integral form, b) it relates the data directly to an arbitrary conductivity distribution and, c) it relies on the relatively simple theory of a homogeneous half-space, but it handles heterogeneous media by adapting its conductivity according to the data, without the need for an initial or reference model. These features are exploited by the 1-D extensions mentioned above in relation to controlled source methods. Extensions to higher dimensions for special types of electromagnetic measurements also profit from them (e.g. Pérez-Flores and Gómez-Treviño, 1997; Pérez-Flores et al., 2001; Brunner et al., 2003; Friedel, 2003). In this paper, we explore the possibilities of the same approach for the two-dimensional (2-D) MT problem.

## THE APPROXIMATION

In the magnetotelluric method, surface measurements of natural time-varying electric and magnetic fields are readily converted to four complex impedance values per given angular frequency ω. In turn, these values are usually normalized to obtain apparent resistivities or, equivalently, apparent conductivities, by referring the actual impedances to those of a homogeneous half-space (Cagniard, 1953). Here we use apparent conductivity $\sigma_a$ as derived from the magnitude of a complex impedance $Z$ which, for the moment, represents any of the four elements of the impedance tensor. The formula for apparent conductivity is simply given as

$$\sigma_a(x,\omega) = \omega\mu_0 \mid Z(x,\omega) \mid^{-2}, \quad (1)$$

where $\mu_0$ stands for the magnetic permeability of free-space and $x$ represents horizontal distance in an $x$-$z$ coordinate system whose $z$ axis represents depth. $\sigma_a(x, w)$ represents the data at a given distance in a 2-D model with a flat topography and for a given angular ω. The data are usually presented as individual sounding curves as a function of period $T = \frac{2\pi}{\omega}$ for different distances $x$, or in a pseudo-section format contouring values of $\sigma_a$ as plotted over $x$-$T$ coordinates. $\sigma_a(x, w)$ represents what is available; what is required is $\sigma(x, z)$, the subsurface conductivity distribution.

A useful relationship between $\sigma_a(x, T)$ and $\sigma(x, z)$ for the problem at hand is (Gómez-Treviño, 1987a):

$$\sigma_a(x,T) = \frac{1}{1-m}\int F(x,x',z',\sigma,T)\sigma(x',z')dx'dz', \quad (2)$$

where:

$$m = \frac{d\log\sigma_a}{d\log T}, \quad (3)$$

and $F(x,x',z',\sigma,T)$ represents the Fréchet derivative of

$\sigma_a(x, T)$ with respect to $\sigma(x, z)$. The integration is defined over the entire lower half-space. The recovery of $\sigma(x, z)$ from $\sigma_a(x, T)$ is clearly a nonlinear problem since $F$ depends on $\sigma$. Otherwise, the integral equation could be readily solved using any of the available methods of linear analysis. It is still possible to apply linear methods sequentially, as in traditional linearization, simply by updating a starting model on the right-hand side of the equation. Esparza and Gómez-Treviño (1996), working with the 1-D problem, showed that reasonably good results can be obtained in a single iteration using an adaptive approximation. In 1-D, the approximation is

$$F(z',\sigma,T) = (1-m)F_h(z',\sigma_a,T). \quad (4)$$

$F(z',\sigma,T)$ on the left hand-side represents the true Fréchet derivative for an arbitrary conductivity distribution, and $F_h(z',\sigma_a,T)$ on the right stands for the much simpler Fréchet derivative of a homogeneous half-space, whose conductivity is known and equal to the measured apparent conductivity. $F_h$ is simply an attenuated cosine function that gradually vanishes with depth. The factor (1-$m$) drops out of the approximation when substituting expression (4) in equation (2). Using the Fréchet derivative $F_h(z',\sigma_a,T)$ for a homogeneous half-space (Gómez-Treviño, 1987b), the approximation in 1-D can be written as

$$\sigma_a(T) = \frac{2}{\delta_a}\int_0^{\infty} e^{-2z'/\delta_a}\left[\cos(\frac{2z'}{\delta_a}) + \sin(\frac{2z'}{\delta_a})\right]\sigma(z')dz', \quad (5)$$

where $\delta_a = 503\sqrt{T/\delta_a}$ . In the original Niblett-Bostick integral equation, the upper limit of integration is $0.707\delta_a$ and the kernel is simply $(0.707\sigma_a)^{-1}$.

To solve equation (5) numerically, we divide the half-space into a large number of layers with uniform conductivities. The result is that the integral equation can be written as a matrix equation

$$\sigma_a = \mathbf{A}\sigma. \quad (6)$$

The vector $\sigma_a$ contains the data for the different periods. The vector σ represents the unknown conductivity distribution in its discrete form, and the matrix **A** contains the weights of the conductivity elements for all the available data. The elements of the matrix can be evaluated analytically as

$$a_{ij} = e^{(-2z_j/\delta_{ai})}\cos(\frac{2z_j}{\delta_{ai}}) - e^{(-2z_{j+1}/\delta_{ai})}\cos(\frac{2z_{j+1}}{\delta_{ai}}), \quad (7)$$

where $z_j$ is the top depth of the *j-th* layer, and $\delta_{ai}$ is the skin depth of the *i-th* measurement.

By analogy, making the same type of assumptions and approximations in 2-D, equation (2) can be written as

$$\sigma_a(x,T) = \int F_h(x,x',z',\sigma_a,T)\sigma(x',z')dx'dz'. \quad (8)$$

Analytical expressions for $F_h$ are derived in Appendix A for the traditional TE and TM modes, respectively. In turn, they are used in Appendix C to derive the corresponding expressions for series and parallel apparent conductivities.

In 2-D, to construct equation (6) the half-space is divided into a large number of rectangular elements. The integration over the elements can be performed analytically as described in Appendix B. This is particularly useful for handling the singularities at the points of measurement, and also for the final rectangles on the sides and bottom of the model. It is worth remarking that each of the elements of $\sigma_a$ is a weighted average of all the unknown conductivity values and, that on virtue of equation (2), the elements of matrix **A** are dimensionless. Furthermore, the sum of the elements of any row of **A** is identically unity, which is a very useful property for checking the accuracy of the computations involved. Notice that although equation (6) is a system of linear equations, the model it represents is actually nonlinear, for **A** depends on the unknown distribution σ through the different values of $\sigma_a$.

## HOPFIELD ARTIFICIAL NEURAL NETWORKS

The application of artificial neural networks to the inversion of MT data has been explored in various directions. One way is to use the multi-layer feed forward neural network architecture (Rummelhart et al., 1986) which uses a set of responses and models presented to the input and output defined neurons, respectively. During a learning phase, the network *back-propagates* (through its neurons and interconnection weights) errors due to misfit of the model and the obtained neural model. Learning from one response-model 'pattern' is achieved by updating the inter neuron connection weights according to a gradient descent minimization criteria. The process is then applied to the complete response-model data set, thereby achieving a learning epoch.

Once the network is trained, it recovers a model in almost no time when provided with a sounding curve. The distinctive feature of this learning approach is that there is very little physics fed into the algorithms. In fact, as far as the algorithms are concerned, the models and responses used in the training sessions may or may not be related through any physical link, the learning process is simply the same. Hidalgo and Gómez-Treviño (1996) explored this approach for the 1-D problem with reasonably good results. However, extending the method to 2-D would be

extremely cumbersome, for it is necessary to cover many possibilities during each epoch training session.

Another approach to inversion based on neural networks bypasses the learning sessions by directly providing the algorithm with the relevant physics behind the particular application. Zhang and Paulson (1997) applied a simple recursive regularization algorithm associated with a Hopfield artificial neural network (HANN) in order to solve the 1-D MT inverse problem with excellent results. In the same paper the authors explored the application to the 2-D full nonlinear inversion of MT data. Our interest in this algorithm was triggered by the fact that there are no references in the literature attempting to continue their research in this direction, even though the results presented are very promising. In this methodology there are no dedicated input-output defined units (as with the feed-forward network architecture). Instead, every neuron $\sigma_i$ is interconnected with every other $\sigma_j$ neuron through a $T_{ij}$ weight link as detailed below. Every neuron has a twofold input-output purpose. We assume $M$ apparent conductivity measurements and $N$ blocks whose conductivities are unknown. According to equation (6), for given conductivity values $\sigma_j$, $j = 1,...,N$, the responses $\hat{\sigma}_{ak}$, $k = 1,...,M$, of the model can be expressed as

$$\hat{\sigma}_{ak} = \sum_{j=1}^{N} a_{kj}\sigma_j, k = 1,...,M. \quad (9)$$

The misfit between $\sigma_{ak}$ (the data) and $\hat{\sigma}_{ak}$, (the model responses) can be written as

$$C = \frac{1}{2}\sum_{k=1}^{M} (\sigma_{ak} - \hat{\sigma}_{ak})^2 = \frac{1}{2}\sum_{k=1}^{M} [\sigma_{ak} - \sum_{j=1}^{N} a_{kj}\sigma_j]^2 \cdot (10)$$

Squaring as indicated and rearranging terms, this expression corresponds to

$$C = -\frac{1}{2}\sum_{i=1}^{N}\sum_{j\neq i=1}^{N}[-\sum_{k=1}^{M} a_{ki}a_{kj}]\sigma_i\sigma_j - \sum_{i=1}^{N}[-\frac{1}{2}\sum_{k=1}^{M} a_{ki}^2\sigma_i + \sum_{k=1}^{M} a_{ki}\sigma_{ak}]\sigma_i + \frac{1}{2}\sum_{k=1}^{M}(\sigma_{ak})^2. \quad (11)$$

It can be noted that this is an unnecessarily long, and certainly very cumbersome way of representing $C$, the sum of squares. However, this particular form helps to recognize its correspondence to

$$E = -\frac{1}{2}\sum_{i=1}^{N}\sum_{j\neq i=1}^{N} T_{ij}\sigma_i\sigma_j - \sum_{i=1}^{N} I_i\sigma_i, \quad (12)$$

where

$$T_{ij} = -\sum_{k=1}^{M} a_{ki}a_{kj} \quad \text{and}$$

$$I_i = -\frac{1}{2}\sum_{k=1}^{M} a_{ki}^2\sigma_i + \sum_{k=1}^{M} a_{ki}\sigma_{ak}. \quad (13)$$

$E$ is the Ising Hamiltonian (Ising, 1925) which Tank and Hopfield (1986) showed is a never increasing quantity as the dynamics defined by the following equation evolve from given starting values:

$$\sigma_i^{(t+1)} = \frac{1}{2} + \frac{1}{2}\mathrm{sgn}\left(\sum_{j\neq i=1}^{N} T_{ij}\sigma_j^{(t)} + I_i\right). \quad (14)$$

$\sigma_j^{(t+l)}$ is the updated conductivity value of $\sigma_j^{(t)}$ which is either a given starting value or the result of a previous iteration. The relevance of dynamic is that as iterations proceed $E$ decreases at each step. Since $E$ corresponds to $C$, the dynamics ensure that the sum of the squared differences between data and model responses decrease at each step, thus leading to the model whose responses best fit the data in a least square sense. It can be noted that with the HANN the matrix elements $T_{ij}$ are known and provided by the physics of the problem, since they are the elements $(A^T A)_{ij}$, which in turn come from the integral equation.

Strictly speaking, equation (14) applies only to binary variables that can take values of zero and one, as in the HANN architecture (Hopfield, 1982). The corresponding equations for an assemblage of such variables, to make up for arbitrary values of conductivity, are very similar and are given in Appendix D.

The application of equation (14) is straightforward when $M>N$, for the process reduces to the standard least squares problem. This corresponds to the over constrained case when we have more data than unknown parameters. In general, however, $M<N$ since there usually are fewer data points than unknowns. We found, as did Zhang and Paulson (1997), that the algorithm still converges even for $M<N$, but the solution is hardly useful for any practical purpose because it is highly oscillatory and unrealistic. It is then necessary to make some extra assumptions about the solution. This issue is addressed in the next section.

## SPATIAL AVERAGES

### True averages

As reviewed in the introductory section above, the methods of Backus and Gilbert allow for the computation of spatial averages. This is done by means of averaging functions constructed as linear combinations of the Fréchet derivatives

of the data in such a way that the averaging functions resemble boxcar functions for the averages to have the usual meaning. The resulting models are not intended to produce responses that fit the data, but to address the non-uniqueness character of the inverse problem. Within the limitations of linearization, they can be called true averages. More rigorous approaches for computing averages have been developed for the 1-D magnetotelluric problem (e.g. Weidelt, 1992), but their extension to higher dimensions are far from trivial.

## Simulated averages

The shortcut that we take consists of computing models that are averages of themselves everywhere with a given neighborhood, and that at the same time their responses fit the data at an optimal level. Consider that

$$\sigma_j^{(t)} = \sum_{l=-n}^{n} w_l \sigma_{(j+l)}^{(t)}. \qquad (15)$$

The dynamics of the HANN in (14) transforms to

$$\sigma_i^{(t+1)} = \frac{1}{2} + \frac{1}{2}\mathrm{sgn}\left\{ \sum_{j\neq i=1}^{N} T_{ij} [\sum_{l=-n}^{n} w_l \sigma_{(j+l)}^{(t)}] + I_i \right\}. \qquad (16)$$

Following Zhang and Paulson (1997), we will refer to this as the regularized version of the HANN or RHANN. The updated conductivities $\sigma_j^{(t+1)}$ are obtained from averages of the original values $\sigma_j^{(t)}$. The choice of the appropriate filter depends on the application. Zhang and Paulson (1997) found binomial filters useful to stabilize their solution. In our case, we use boxcar functions, for this leads to the simplest and most intuitive type of averages. The filter, with $2n+1$ uniform weights $w_k = (2n+1)^{-1}$, k = -n,..., n (square window), can be of different widths. We introduce a further parameter $\beta$ to accommodate a traditional trade-off between two contrasting features. We modified the dynamics to

$$\sigma_i^{(t+1)} = \frac{1}{2} + \frac{1}{2}\mathrm{sgn}\{ \sum_{j\neq i=1}^{N} [(1-b) T_{ij} \sigma_j^{(t)} + \beta \sum_{l=-n}^{n} T_{ij} w_l \sigma_{(j+l)}^{(t)}] + I_i \}. \qquad (17)$$

When $\beta$=1 we get the full filtered solution. On the other hand, when $\beta$=0 we return to the original unfiltered solution given by equation (14). In this way, by varying this parameter we can gradually control the effect of the averaging process.

# APPLICATIONS

## 1-D averages

Before proceeding to the application in 2-D of the above numerical averaging technique, it is convenient to illustrate its performance in 1-D, and compare its results with existing methods of average estimations. In the following lines, we test the performance of equation (16) as it applies to the solution of equation (6). The elements of the matrix are computed using equation (7) which represents the 1-D version of the proposed approximation. The synthetic data for the tests, shown in Fig. 1A, correspond to apparent conductivity responses of the model shown in Fig. 1B.

The tests are intended to demonstrate that the proposed approach for the computation of averages has the same properties as the simple formula for averages in Gómez-Treviño (1996). The formula is

$$< \sigma(z_1, z_2) >= \frac{\sigma_a(T_2)\delta_a(T_2) - \sigma_a(T_1)\delta_a(T_1)}{\delta_a(T_2) - \delta_a(T_1)}, \qquad (18)$$

where $<\sigma(z_1,z_2)>$ represents the average of conductivity between $z_i = 0.707\delta_a(T_i), i$ = 1,2. The averages are assigned to the mean geometrical depth $z = \sqrt{z_1 z_2}$. Any two data points can be used in the formula regardless of how far apart they are in the sounding curve. If the points are contiguous, the windows are narrow and the average model, the average of the real earth, has the highest possible resolution. If, on the other hand, the chosen points are wide apart, the windows are themselves wide, for $z_1$ and $z_2$ tend to separate. As the windows widen, the models tend to flatten, as they should. This intuitively appealing feature of spatial averages is built into equation (18) in spite of its simplicity. Figures 1C and 1D show this feature developing when considering averages taken from data values 1 and 5 periods apart, respectively, for the synthetic data presented in Fig. 1A.

A corresponding sequence of full filtered models ($\beta$=1) is presented in Figs. 1E and 1F when the RHANN algorithm is applied to the same set of data. It can be observed that the behavior of the averages follows that of the averages shown in Figs. 1C and 1D. There are some differences that can be traced back to basic differences between the two approaches. One is that equation (18) is based on the original Niblett-Bostick approximation that assumes a boxcar function as the kernel of equation (5). The RHANN algorithm uses the kernel as indicated in equation (5) which includes a small negative sidelobe (Gómez-Treviño, 1987b) and extends to infinity. This is a somewhat less restrictive approximation than the rather simpler boxcar function. The other difference originates in the fact that the windows in each approach are necessarily different, because in the first case they cannot be uniform, for they are determined by the data, and in the second case they are uniform for all depths. The overall effect is a somewhat better performance for the approximation given by equation (5) judging by the resemblance of the average models to the original model from which the data were drawn.

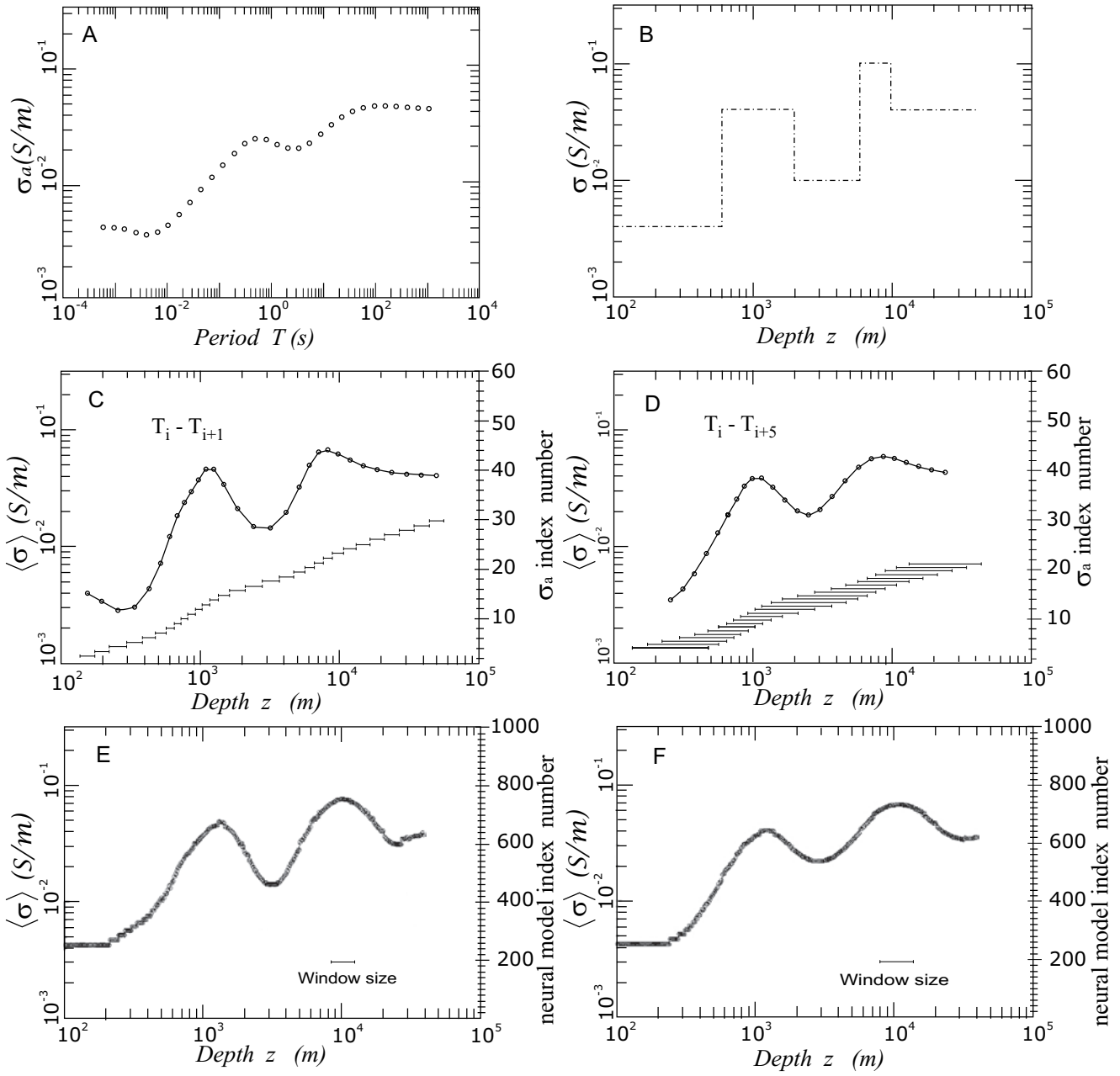


FIGURE 1 | **A) Synthetic data for test model. B) Test model. C) Recovery of test model using the average approach given by equation (18). $T_1$ and $T_2$ are chosen as follows: $T_i$-$T_{i+1}$. D) Using $T_i$-$T_{i+5}$ . Notice the smoothing effect on the models as the averaging windows widen. The windows, shown below the model, are nonuniform because they depend on the data whose index is shown in the right axis. E) and F) show the recovery of full filtered test models ($\beta$ = 1) using a 500 layer RHANN. In this case, the window size is chosen at will corresponding to a uniform window size in *log* depth (i.e., the same averaging window size for the 500 layers). Notice the same overall behavior of the average models as compared with those in Figures 1C and 1D, respectively.**

More appealing from the practical point of view, is the stabilizing property of the averages when applied to noisy data. When equation (18) is applied to noisy data using contiguous data points, which is equivalent to using the original Niblett-Bostick transformation in terms of slopes, the estimation of the conductivity profile is very unstable. This is equivalent to the use of a narrow window, which understandably leads to a noisy recovery of a conductivity profile. Increasing the width of the window improves the stability of the recovered profile. This is illustrated in Fig. 2, which presents the results of applying equation (18) to the noisy data shown in Fig. 2A. The natural regularizing effect that the wider windows have on the recovered profiles can be observed in Figs. 2C and 2D. The results of applying the RHANN algorithm to the same set of data are shown in Fig. 2E and 2F. The sequence of models illustrates the evolution of the process as the windows are widened, reaching a reasonably good recovery with the widest window.

The above results show that the RHANN algorithm mimics the performance of equation (18) when applied to 1-D sounding data. First, we have that the simulated averages actually behave as true averages, with the added benefit that the RHANN algorithm allows more freedom in choosing the size of the windows, for they can be chosen at will and are independent of how the data were sampled. Second, we have the same type of regularization effect as provided by equation (18), when the algorithm is applied to noisy data. In both instances, the main benefit of the RHANN algorithm is that it can be readily applied to higher dimensions.

## Two-dimensional averages

The problem at hand can be summarized as follows: evaluate the performance of equations (16) and (17) as they apply to the solution of equation (6), where the elements of

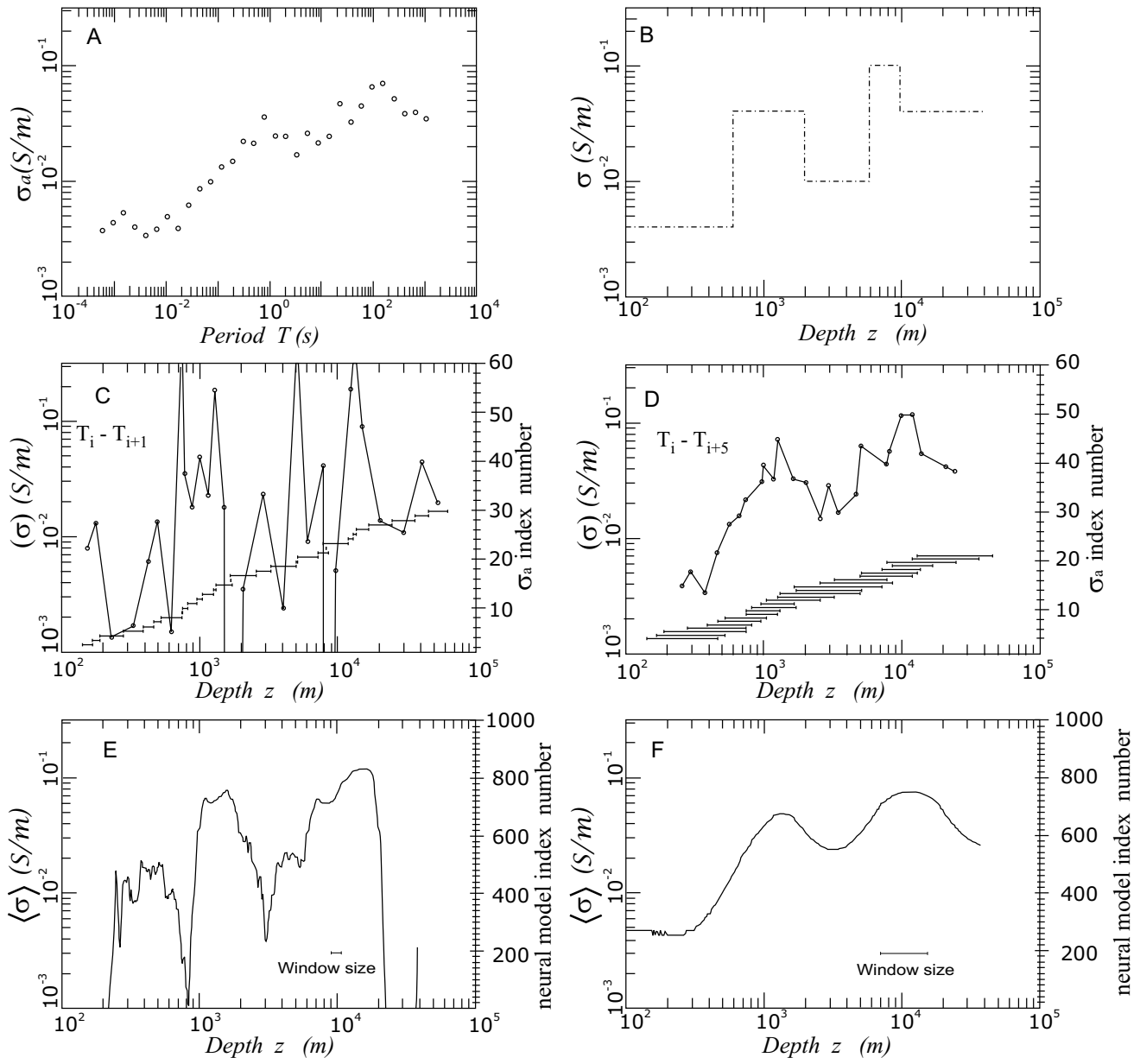


FIGURE 2 | **A) Synthetic data with 5% noise added to test model. B) Test model. C) Recovery of test model using the average approach given by equation (18). $T_1$ and $T_2$ are chosen as follows: $T_i$-$T_{i+1}$ . D) Using $T_i$-$T_{i+5}$ . Notice the smoothing effect on the models as the averaging windows widen. The windows, shown below the model, are non-uniform because they depend on the data whose index is shown in the right axis. Figures E) and F) show the recovery of full filtered test models ($\beta$ = 1) using a 500 layer RHANN. In this case, the window size is chosen at will, corresponding to a uniform window size in *log* depth (i.e., the same averaging window size for the 500 layers). Notice the same overall behavior of the average models as compared with those in Figures 2C and 2D, respectively.**

the matrix are computed for 2-D on the basis of equation (8), as developed in Appendix C. The evaluation is effected first using synthetic data sets and then employing the standard COPROD2 (Jones, 1993) data set. For the case of synthetic data, we generate a 2-D mesh array discretization consisting of 21 lines and 60 columns in which we embedded resistive and conductive blocks as shown in Fig. 3A. Figures 3B and 3C present average models derived by convolving the original model with the two windows indicated in each case. The object of the exercise is to recover the average models from a given set of synthetic data. Twenty-nine soundings at the indicated sites were simulated in the period range of 0.01 to 100 s. The TM and TE impedances were converted to corresponding series and parallel quantities using equations (C7) and (C8).

Figure 4A shows the resultant model obtained when using the RHANN algorithm. This result was achieved after a 'stable' state of the dynamics was reached, when a uniform half-space of resistivity ρ=10 Ω·*m* was used as an initial condition for each neuron state. Figure 4B shows the model obtained when a different uniform half-space of ρ=1 Ω·*m* was used as an initial condition. Graphics 4A and 4B were obtained using both series and parallel data. It can be observed that the models are practically identical, as they should be, for the need of an initial state is an internal requirement of the HANN algorithm and not of the formulation of the inverse problem as given by equation (6). It can also be noted that the conductive block is better resolved than the resistive one, as could be expected from the known features of the Niblett-Bostick approximation as well as from the basic properties of electromagnetic induction in general. We found that it is still possible to emphasize either the resistor or the conductor by choosing the data to be inverted. The series response is more representative of resistors while conductors are better reflected in the parallel data (Romo et al., 2005). This is illustrated in Fig. 5 for the case of the resistor and in Fig. 6 for the case of the conductor. In the preceding figures, and in the ones that follow, the *rms* values shown on top of the models were computed as 100 times the square root of the mean of the residuals squared. The residuals are simply the difference between the data and the computed response of the model given by equation (6), normalizing each difference by the corresponding computed response.

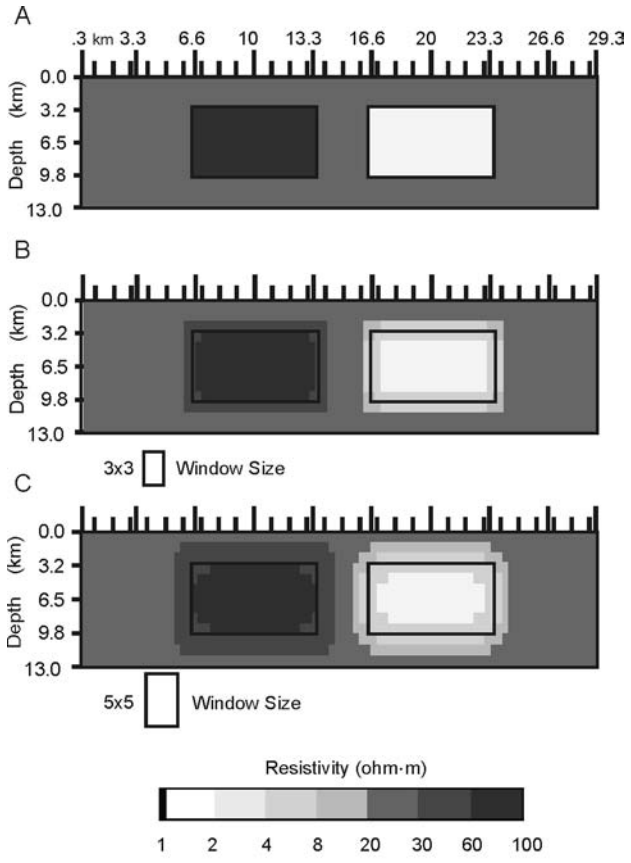


FIGURE 3 | **A) Two-dimensional test model. B) and C) Average models obtained when the window shown at the right is applied to the original model. These average models are the target of the RHANN approach.**

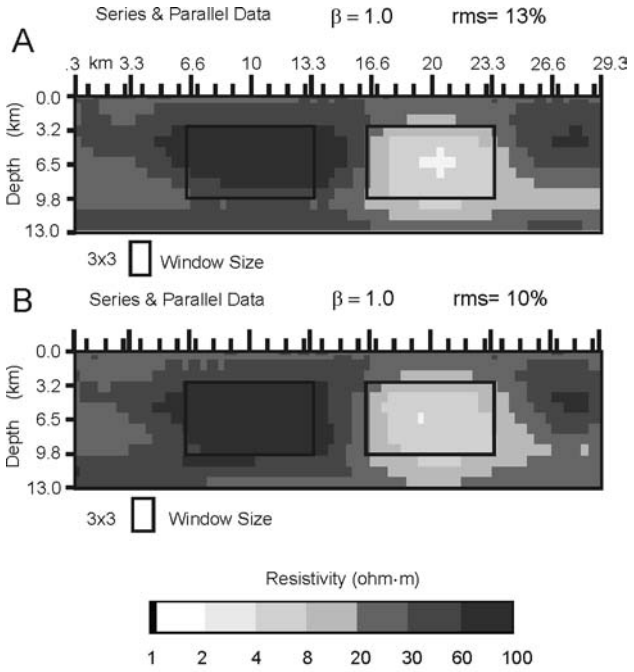


FIGURE 4 | **A) Resultant model obtained when using the regularized Hopfield artificial neural network (RHANN). This result was achieved after a stable state of the dynamics was reached, when uniform half-space of resistivity $\rho$ = 10 Ω·*m* was used as an initial condition for each neuron state. B) Model obtained when a different initial condition is used. In this case a half-space of $\rho$ = 1 Ω·*m* was used. The above graphics were obtained using both series and parallel data.**

We now turn to illustrate the performance of the algorithm with field data. The data corresponds to the original COPROD2 (Jones, 1993) data set, with no

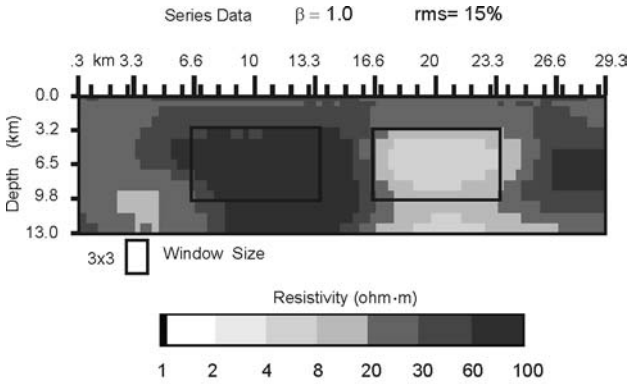


FIGURE 5 | **Model obtained by means of the RHANN, when using data from the series mode only with a 3×3 window size and $\beta$ = 1.0 . It can be seen that the series-based inversion emphasizes the resistivity nature of the anomalies.**

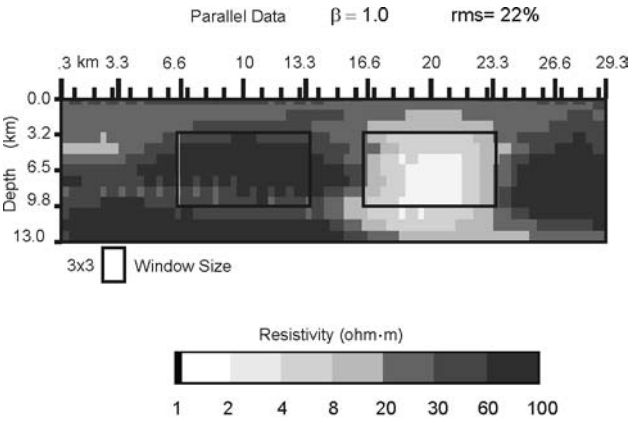


FIGURE 6 | **Model obtained by means of the RHANN, when using data from the parallel mode with only a 3×3 window size and $\beta$ = 1.0. It can be seen that the parallel-based inversion emphasizes the conductive nature of the anomalies.**

corrections for static effects. The full tensor was used to compute the invariant *series and parallel* impedances using equations (C3) and (C4). We used 34 sounding sites with 22 periods each, for a total of 748 apparent conductivity values. The range of periods was from 1.3 s to 1365 s. This same data set was recently inverted by Romo et al. (2005) using Rodi and Mackie (2001) inverse code adapted for series and parallel data. The model shown in Fig. 7 presents two main conductive anomalies. The deeper anomaly to the left of the model corresponds to the North American Central Plains (NACP) conductivity anomaly, which has been discussed in detail in the magnetotelluric literature (Jones, 1993). The smaller lobular anomaly towards the right end of the profile corresponds in turn to the Thomson Nickel Belt (TOBE) anomaly.

The challenge for the proposed 2-D Niblett-Bostick approximation is the recovery of these two anomalies. The model was discretized using a 36×70 mesh array for a total of 2,310 conductivity unknowns. Using 22 bits to represent

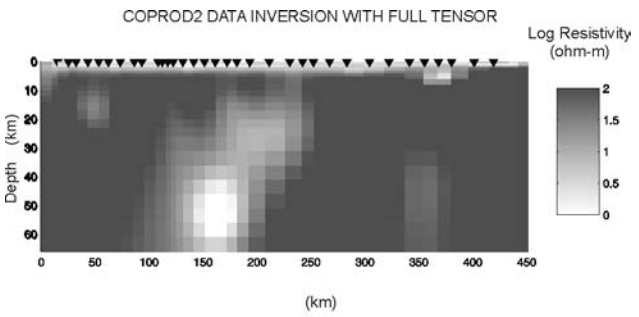


FIGURE 7 | **Model obtained by means of the Rodi and Mackie (2001) non-linear inverse method adapted for series and parallel data (Romo et al., 2005) when applied to the COPROD2 (Jones, 1993) standard data set.**

each unknown, the 748x2,310 matrix took 20 min to compute in an AMD Athlon 1.2 GHz processor, with 20 extra minutes for the minimization. Figure 8A shows the result of jointly inverting the series and parallel data. It can be observed that the approximation clearly recovers

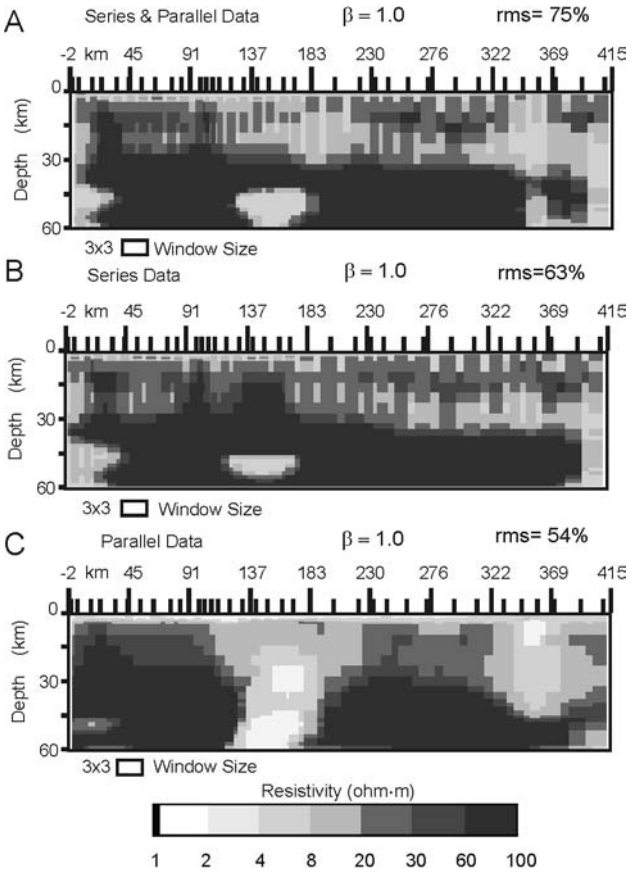


FIGURE 8 | **Models obtained by the RHANN algorithm when applied to the COPROD2 (Jones, 1993) standard data set. A) Result obtained using data from series and parallel modes. B) Result obtained using data from the series mode only. C) Result obtained using data from the parallel mode only.**

only the NACP anomaly. The TOBE anomaly is somehow diluted towards the right side of the model. The results are somewhat similar when only series data are inverted, as can be observed in Fig. 8B. The main difference is that in this last case, the NACP anomaly decreases to about half the size because of the removal of the parallel data which, as mentioned above, tends to emphasize conductors. This effect is explicitly shown in Fig. 8C, where only parallel data were used in the inversion. Both conductive anomalies are now clearly manifested, in reasonable agreement with the model shown in Fig. 7, which does not depend on the approximation. Notice also that, of the three models of Fig. 8, the one for the parallel data has the least *rms* misfit. Still, a level of 52% misfit might seem too large. A corresponding model with a 22% misfit is shown in Fig. 9A. This was obtained simply by lowering the trade-off parameter from 1 to ½. As expected, the higher-resolution model now includes smaller scale anomalies, but the same two main conductors still dominate the picture. Thus, summarizing, when in search of conductors as in most MT surveys, we should feed the approximation with parallel data, which emphasize conductors.

To test the robustness of the algorithm we perturbed the data by multiplying each sounding curve by a random factor of 60% to simulate the static shift effect produced by small local variations in conductivity around the sounding sites. The results are shown in Fig. 9B. The reference model is the same high-resolution model described in the previous paragraph, it is shown in Fig. 9A and has a misfit of 22%. When the soundings were perturbed by 60% the best fit achieved was 40%, much better than an expected

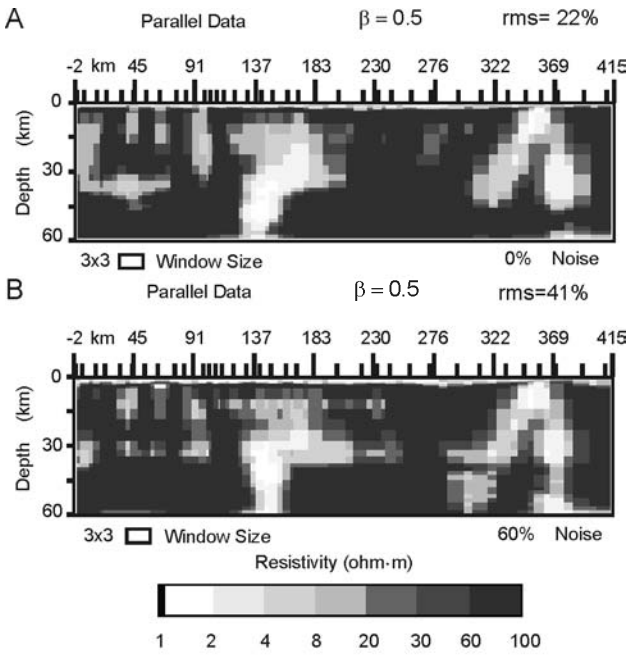


FIGURE 9 | **Models obtained by the RHANN algorithm when random noise was added to the individual sounding curves of the COPROD2 standard data set to simulate static shift effects. The models were obtained using data from the parallel mode. A) 0% of random noise added to data. B) 60% of random noise added to data.**

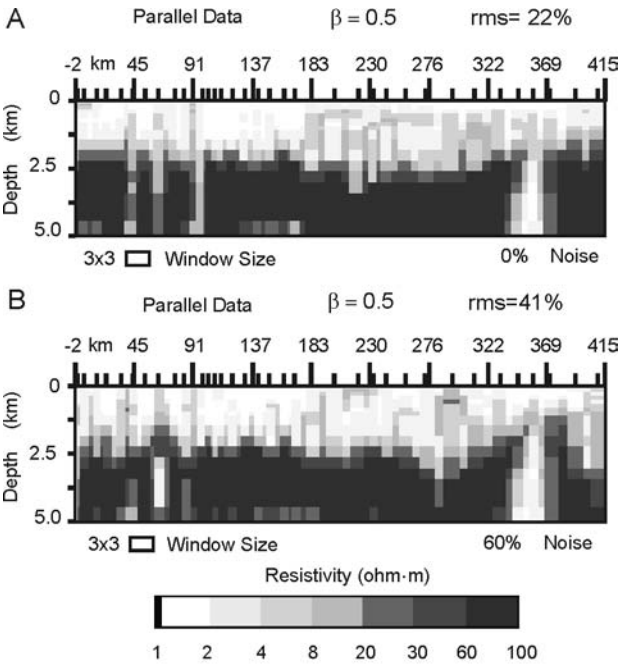


FIGURE 10 | **Zoom view of the first 5 km for the models shown in Figure 9.**

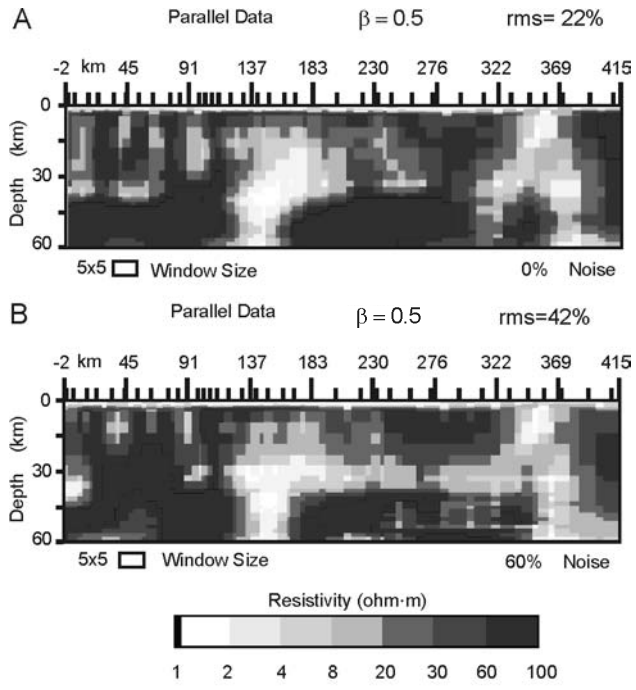


FIGURE 11 | **Same as for Figure 9 but using a wider window.**

80% if the algorithm could not accommodate the static shift into the structure. As can be observed in Fig. 9B, the model for the perturbed data presents basically the same broad features of the two main conductive anomalies. The static shift is accommodated mainly by means of extra variations of conductivity at shallow depths, as expected. This is highlighted in Fig. 10 that shows a zoom view of the first 5 km of the model. The static shift surfaces as high frequency lateral features, over the already highly variable top conductive surface layer. Similar results, with somewhat broader features, are obtained with a larger window. This is illustrated in Fig. 11 for the complete model, with and without extra static contamination.

## CONCLUSIONS

The present application builds on the well-known Niblett-Bostick approximation for 1-D soundings. Our intention has been to show that such an approximation is viable in higher dimensions, both on theoretical and practical grounds. Most quantities involved are analytical as far as they can be; the use of series and parallel impedances avoid elaborated processing of the data prior to interpretation and the RHANN square window approach allows for the computation of averages in a simple fashion. We feel that these features can make the present approximation a fair extension of the popular Niblett-Bostick transformation. Parallel impedances, in particular, are recommended as standard practice for the approximation.

## ACKNOWLEDGMENTS

We would like to thank Colin Farquharson and Josef Pek for their comments and suggestions for improving the manuscript. Joel Rodríguez-Ramírez thanks the Consejo Nacional de Ciencia y Tecnología México (CONACYT) for funding his doctoral studies (scholarship #94748). We also thank CONACYT for Grant #47922.

## REFERENCES

Anderson, W.L., 1975. Improved digital filters for evaluating Fourier and Hankel transform integrals. United States Geological Survey Report USGS-GD-75-012., 223 pp.

Backus, G.E., Gilbert, J.F., 1968. The resolving power of gross earth data. Geophysical Journal of the Royal Astronomical Society, 16, 169-205.

Backus, G.E., Gilbert, J.F., 1970. Uniqueness in the inversion of inaccurate gross earth data. Philosophical Transactions of the Royal Society of London, A266, 123-192.

Bailey, R.C., 1970. Inversion of the geomagnetic induction problem. Proceedings of the Royal Society of London, A315, 185-194.

Boerner, D.E., Holladay, J.S., 1990. Approximate Fréchet derivatives in inductive electromagnetic soundings. Geophysics, 55, 1589-1595.

Bostick, F.X., 1977. A simple almost exact method of magnetotelluric analysis. In: Ward, S. (ed.). Workshop on Electrical Methods in Geothermal Exploration. United States Geological Survey, Contract Nº. 14080001-G-359, 174-183.

Brunner, I., Friedel, S., Jacobs F., Danckwardt, E., 2003. Investigation of a tertiary maar structure using three-dimensional resistivity imaging. Geophysical Journal International, 136, 771-780.

Cagniard, L., 1953. Basic theory of the magneto-telluric method of geophysical prospecting. Geophysics, 18, 605-635.

Christensen, N.B., 1997. Electromagnetic subsurface imaging - A case for an adaptive Born approximation. Surveys in Geophysics, 18, 441-510.

De Groot-Hedlin, C.D., Constable, S.C., 1990. Occam's inversion to generate smooth, two-dimensional models from magnetotelluric data. Geophysics, 55, 1613-1624.

Esparza, F.J., 1991. Sufficiency of Maxwell's equations in relation with electromagnetic inverse problems. Doctoral thesis. México, Centro de Investigación Científica y de Educación Superior de Ensenada, 90 pp.

Esparza, F.J., Gómez-Treviño, E., 1996. Inversion of magnetotelluric soundings using a new integral form of the induction equation. Geophysical Journal International, 127, 452-460.

Friedel, S., 2003. Resolution, stability and efficiency of resistivity tomography estimated from a generalized inverse approach. Geophysical Journal International, 153, 305-316.

Gómez-Treviño, E., 1987a. Nonlinear integral equations for electromagnetic inverse problems. Geophysics, 52, 1297-1302.

Gómez-Treviño, E., 1987b. A simple sensitivity analysis of time-domain and frequency-domain electromagnetic measurements. Geophysics, 52, 1418-1423.

Gómez-Treviño, E., 1996. Approximate depth averages of electrical conductivity from surface magnetotelluric data. Geophysical Journal International, 127, 762-772.

Hidalgo, H., Gómez-Treviño, E., 1996. Application of constructive learning algorithms to the inverse problem. Institute of Electrical and Electronics Engineers (IEEE), Transactions on Geoscience and Remote Sensing, 34, 874-885.

Hohmann, G.W., 1971. Electromagnetic Scattering by conductors in the earth near a line source of current. Geophysics, 36, 101-131.

Hopfield, J.J., 1982. Neural Networks and physical systems with emergent collective computational abilities. United States of America, Proceedings of the National Academy of Sciences, 79, 2554-2558.

Ising, E., 1925. Beitrag zur theorie des ferromagnetismus. Zeitschrift für Physik, 31, 253-258.

Jones, A.G., 1983. On the the equivalence on the Niblett and Bostick transformation in the magnetotelluric method. Journal of Geophysics, 53, 72-73.

Jones, A.G., 1993. The COPROD2 dataset: Tectonic setting, recorded MT data, and comparison of models. Journal of Geomagnetism and Geoelectricity, 45, 933-955.

Lee, K.H., Morrison, H.F., 1980. A solution for TM-mode plane waves incident on a two-dimensional inhomogeneity. Berkeley, Lawrence Berkeley Laboratory, Rep. LBL-10649. 33 pp.

Lee, K.H., Morrison, H.F., 1985. A Solution for TM-mode plane waves incident on a two-dimensional inhomogeneity. Geophysics, 50, 1163-1165.

Niblett, E.R., Sayn-Wittgenstein, C., 1960. Variation of electrical conductivity with depth by the magnetotelluric method. Geophysics, 25, 998-1008.

Oldenburg, D.W., 1979. One-dimensional inversion of natural source magnetotelluric observations. Geophysics, 44, 1218-1244.

Parker, R.L., 1983. The magnetotelluric inverse problem. Geophysical Surveys, 6, 5-25.

Pérez-Flores, M.A., Gómez-Treviño, E., 1997. Dipole-dipole resistivity imaging of the Ahuachapán-Chipilapa geothermal field, El Salvador. Geothermics, 26, 657-680.

Pérez-Flores, M.A., Méndez-Delgado, S., Gómez-Treviño, E., 2001. Imaging of low-frequency and DC electromagnetic fields using a simple linear approximation. Geophysics, 66, 1067-1081.

Rodi, W.L., 1989. Regularization and Backus-Gilbert estimation in nonlinear inverse problems: Application to magnetotellurics and surface waves. Doctoral thesis. Pennsylvania, Pennsylvania State Universitytate University, 297 pp.

Rodi, W., Mackie, R.L., 2001. Nonlinear Conjugate gradients algorithm for 2-D magnetotelluric inversion. Geophysics, 66, 174-187.

Romo, J.M., Gómez-Treviño, E., Esparza, F., 2005. Series and parallel transformations of the magnetotelluric impedance tensor: theory and applications. Physics of the Earth and Planetary Interiors, 150, 63-83.

Rummelhart, D.E., Hinton, G.E., Williams, R.J., 1986. Learning internal representation by backpropagating errors. Nature, 332, 533-536.

Smith, J.T., Booker, J.R., 1988. Magnetotelluric inversion for minimum structure. Geophysics, 53, 1565-1576.

Smith, R.S., Edwards, R.N., Buselli, G., 1994. An automatic technique for presentation of coincident-loop, impulse response, transient, electromagnetic data. Geophysics, 59, 1542-1550.

Swift, C.M., 1967. A magnetotelluric investigation of an electrical conductivity anomaly in the southwestern United States. Doctoral thesis. Massachusetts, Massachusetts Institute of Technology, 211 pp.

Tank, D.W., Hopfield, J.J., 1986. Simple neural optimization networks: An A/D converter, signal decision circuit, and linear programming circuit. Institute of Electrical and Electronics Engineers (IEEE), Transactions on Circuits and Systems, 33, 535-541.

Wait, J.R., 1962. Electromagnetic waves in stratified media. Oxford, The MacMillan Company, 372 pp.

Weidelt, P., 1972. The inverse problem of geomagnetic induction. Journal of Geophysics, 38, 257-289.

Weidelt, P., 1975. Inversion of two-dimensional conductivity structures. Physics of the Earth and Planetary Interiors, 10, 282-291.

Weidelt, P., 1992. Exact and approximate bounds on spatial averages of the electrical conductivity using a priori information. Wellington (New Zealand), Abstracts 11th International Association of Geomagnetism and Aeronomy (IAGA), Workshop on Electromagnetic Induction in the Earth, 5.14-5.15.

Zhang, Y., Paulson, K.V., 1997. Magnetotelluric inversion using regularized Hopfield neural networks. Geophysical Prospecting, 45, 725-743.

**Manuscript received April 2007;**
**revision accepted December 2008;**
**published Online November 2009.**

# APPENDIX

## 1 Fréchet Derivatives

In this appendix we develop formulae for the 2-D Fréchet derivatives of apparent conductivity for a homogeneous half-space. We assume $e^{i\omega t}$ for time dependence in the fields. The definition of apparent conductivity in terms of the fields for the TE mode is:

$$|\sigma_a| = \omega\mu_0 \left|\frac{H_x(x,0)}{E_y(x,0)}\right|^2, \quad (A.1)$$

perturbing the conductivity distribution σ(x,z) produces perturbations on both sides of this equation. We have

$$\delta|\sigma_a| = -2|\sigma_a|\,\mathrm{Re}\left[\frac{\delta E_y(x,0)}{E_y(x,0)} - \frac{\delta H_x(x,0)}{H_x(x,0)}\right]. \quad (A.2)$$

We will need $E_y(x,z)$ and $H_x(x,z)$. To find $E_y(x,z)$ we have to solve the following differential equation:

$$\nabla^2 E_y - i\omega\mu_0\sigma(x,z)E_y = 0, \quad (A.3)$$

for the case of a homogeneous half-space. The solution is simply

$$E_y(x,z) = E(0)e^{-\sqrt{2i}\frac{z}{\delta}}, \quad (A.4)$$

where δ is the skin depth, given by

$$\delta^2 = \frac{2}{\omega\mu_0\sigma}. \quad (A.5)$$

In what follows, all the distances are normalized by the skin depth. $H_x(x,z)$ can be found using Maxwell's equation $\nabla\times\mathbf{E} = -\mathbf{i}\omega\mu_0\mathbf{H}$, the result is

$$H_x(x,z) = \frac{1}{i\omega\mu_0\delta}\frac{\partial}{\partial z}E_y(x,z). \quad (A.6)$$

Using equation (A4), the horizontal magnetic field can be written as

$$H_x(x,z) = \frac{-\sqrt{2i}}{i\omega\mu_0\delta}E(0)e^{-\sqrt{2i}z}. \quad (A.7)$$

To find $\delta E_y(x,0)$ we use the scattering relation (Hohmann, 1971; Weidelt, 1975) which, for TE mode, reduces to

$$\delta E_y(x,0) = \int G(x,0;x',z')E_y(x',z')\delta\sigma(x',z')dx'dz'. \quad (A.8)$$

In this equation, $G$ is the $y$ component of the electric field at $(x,0)$ produced by a line source of alternating current located at $(x',z')$ and parallel to the $y$ axis. The expression for $G$ can be found in Wait (1962) and is

$$G(x,z;x',z') = \frac{-i\omega\mu_0}{2\pi}\int_0^\infty \left[\frac{u-\lambda}{u+\lambda}e^{-u(z+z')} + e^{-u|z-z'|}\right] \times \frac{\cos[\lambda(x-x')]}{u}d\lambda, \quad (A.9)$$

with $u^2 = \lambda^2 + 2i$. To find $\delta H_y(x,0)$ we take perturbations on both sides of equation (A6), the result is

$$\delta H_x(x,0) = \frac{1}{i\omega\mu_0\delta}\frac{\partial}{\partial z}\delta E_y(x,z)|_{z=0}. \quad (A.10)$$

Finally, using equations (A2), (A8) and (A10), we find the Fréchet derivative in terms of the normalized distances. For TE mode:

$$G^{TE} = \mathrm{Re}\left[\frac{2}{\pi\delta^2}\int_0^\infty G_\lambda^{TE}\cos[\lambda(x-x')]d\lambda\right], \quad (A.11)$$

where

$$G_\lambda^{TE} = \frac{\lambda + i(2+\lambda)}{\lambda+u}e^{-(u+\sqrt{2i})z'}. \quad (A.12)$$

For TM mode apparent conductivity is given by

$$|\sigma_a| = \omega\mu_0\left|\frac{H_y(x,0)}{E_x(x,0)}\right|^2. \quad (A.13)$$

Taking perturbations on both sides of this equation, we find

$$\delta|\sigma_a| = -2|\sigma_a|\,\mathrm{Re}\left[\frac{\delta E_x(x,0)}{E_x(x,0)} - \frac{\delta H_y(x,0)}{H_y(x,0)}\right]. \quad (A.14)$$

In the above equation, since $\delta H_y$ is zero, we have to find $\delta E_x$ only. For this we use the scattering relations given by Lee and Morrison (1985):

$$dE_x(x,z) = \int (g_{11}, g_{12}, g_{13})\mathbf{E}(x',z')\delta\sigma(x',z')dx'dz'. \quad (A.15)$$

$g_{ij}$ is the $j$-component of the electric field in $(x,z)$ produced by a 2-D oscillating electric dipole located in $(x', z')$ and

oriented in the *i* direction. On the other hand, the horizontal magnetic field satisfies the following differential equation

$$\nabla^2 H_y - i\omega\mu_0\sigma H_y = -\frac{1}{\rho}\nabla H_y \times \nabla\rho. \quad \text{(A.16)}$$

The solution of this equation for a homogeneous half-space is simply

$$H_y(x,z) = H(0)e^{-\sqrt{2i}z}. \quad \text{(A.17)}$$

Therefore, the horizontal electric field is given by

$$E_x(x,z) = \frac{H(0)\sqrt{2i}}{\sigma\delta}e^{-\sqrt{2i}z}. \quad \text{(A.18)}$$

Since **E** for TM mode is $(E_x,0,E_z)$ and for a homogeneous half-space $E_z$ is zero, we only need $g_{11}$ to compute $\delta E_x$. The expression for $g_{11}$ is given in Lee and Morrison (1980).

$$g_{11}(x,z;x',z') = \frac{-1}{2\pi\sigma\delta^2}\int_0^\infty u[e^{-u|z-z\uparrow} + e^{-u(z+z')}] \times \cos[\lambda(x-x')]d\lambda. \quad \text{(A.19)}$$

Combining equations (A14), (A15), (A18), and (A19), we find the Fréchet derivative for TM mode:

$$G^{TM} = \mathrm{Re}[\frac{2}{\pi\delta^2}\int_0^\infty ue^{-(u+\sqrt{2i})z'}\cos[\lambda(x-x')]d\lambda]. \quad \text{(A.20)}$$

## 2 Integral of Fréchet derivatives for TE and TM modes

Here we find the integral of the Fréchet derivatives for a typical cell. For TE mode we integrate equation (A11) in the region $x_i \le x' \le x_{i+1}$, $z_j \le z' \le z_{j+1}$. That is

$$I_{TE} = \int_{z_j}^{z_{j+1}}\int_{x_i}^{x_{i+1}} \delta^2 G^{TE}(x,x',z')dx'dz'. \quad \text{(B.1)}$$

The result is

$$I_{TE} = \frac{2}{\pi}\int_0^\infty \frac{\lambda + i(\lambda+2)}{\lambda(u+\lambda)(u+\sqrt{2i})}[e^{-(u+\sqrt{2i})z_{j+1}} - e^{-(u+\sqrt{2i})z_j}] \times [\sin[\lambda(x-x_{i+1})] - \sin[\lambda(x-x_i)]]d\lambda. \quad \text{(B.2)}$$

For TM mode we integrate equation (A20) in the same region, the result is

$$I_{TM} = \frac{2}{\pi}\int_0^\infty \frac{u}{\lambda(u+\sqrt{2i})}[e^{-(u+\sqrt{2i})z_{j+1}} - e^{-(u+\sqrt{2i})z_j}] \times [\sin[\lambda(x-x_{i+1})] - \sin[\lambda(x-x_i)]]d\lambda. \quad \text{(B.3)}$$

The integrals $I_{TE}$ and $I_{TM}$ as defined by Eqs. (B2) and (B3) are complex numbers. However, the real part of each one represents the corresponding integral of the Fréchet derivate of $|\sigma_a|$. The horizontal axis is divided into *n* elements, from $x_1$ to $x_m$, and the vertical distance is divided into *m* elements, from $z_1$ to $x_m$, then Eqs. (B2) and (B3) can be used to find the integral of the Fréchet derivative in the rectangular region defined by $[x_i, x_{i+1}]$, and $[z_i, z_{i+1}]$. To take into account the whole half-space we have to consider $(-\infty, x_1]$ and $[x_n, +\infty)$ in the horizontal coordinate and $[z_m, +\infty)$ in the vertical coordinate. The first case can be computed by noting that the corresponding sine transform for the argument $x-b$ with $b\to\pm\infty$ is zero. The second case can be easily computed, considering that the corresponding exponential in equations (B2) or (B3) is null. In all cases, the actual computations are performed using the digital filters for sine and cosine transforms of Anderson (1975). Further details are available in the thesis of Esparza (1991).

## 3 Series and parallel impedances and their derivatives

### *The series-parallel transformation*

The horizontal components of the electromagnetic field are linearly related through a second order impedance tensor (e.g., Swift, 1967). That is,

$$\begin{pmatrix} E_x \\ E_y \end{pmatrix} = \begin{pmatrix} Z_{xx} Z_{xy} \\ Z_{yx} Z_{yy} \end{pmatrix}\begin{pmatrix} H_x \\ H_y \end{pmatrix}, \quad \text{(C.1)}$$

where $Z_{xx}$, $Z_{xy}$, $Z_{yx}$ and $Z_{yy}$ are complex numbers. $E_x$, $Z_y$ are the orthogonal components of the electric field and $H_x$, $H_y$ are the corresponding magnetic field components. Following the work of Romo et al. (2005), we use an alternative representation defined by the following transformation

$$\{Z_{xx}, Z_{xy}, Z_{yx}, Z_{yy}\} \Leftrightarrow \{Z_S, Z_P, \bar{\theta}, \Delta\theta\}, \quad \text{(C.2)}$$

where

$$Z_S = (\frac{Z_{xx}^2 + Z_{xy}^2 + Z_{yy}^2 + Z_{yx}^2}{2})^{1/2}, \quad \text{(C.3)}$$

$$Z_P = \sqrt{2}\frac{Z_{yx}Z_{xy} - Z_{xx}Z_{yy}}{(Z_{xx}^2 + Z_{xy}^2 + Z_{yy}^2 + Z_{yx}^2)^{1/2}}, \quad \text{(C.4)}$$

$$\overline{\Delta\theta} = \arctan(\frac{Z_{xx} + Z_{yy}}{Z_{xy} - Z_{yx}}), \quad \text{(C.5)}$$

$$\bar{\theta} = \frac{1}{2}\arctan(\frac{Z_{yy} - Z_{xx}}{Z_{xy} + Z_{yx}}). \quad \text{(C.6)}$$

If we consider a 2-D case in which the magnetotelluric responses are solely characterized by $Z_{TM} = Z_{xy}$ and $Z_{TE} =$

$Z_{yx}$ modes, we have that $\Delta\theta = 0$, and $\theta$ is simply the strike direction. $Z_S$ and $Z_P$, the series and parallel impedances, respectively, can be written as

$$Z_S^2 = \frac{1}{2}(Z_{TM}^2 + Z_{TE}^2), \tag{C.7}$$

and

$$\frac{1}{Z_P^2} = \frac{1}{2}(\frac{1}{Z_{TM}^2} + \frac{1}{Z_{TE}^2}). \tag{C.8}$$

### *Series impedance derivative*

We can express the series apparent resistivity $\rho_a^S$ in terms of the TE and TM apparent resistivities as

$$\rho_a^S = \frac{1}{2}(\rho_a^{TM} + \rho_a^{TE}), \tag{C.9}$$

in this equation the three apparent resistivities are complex quantities. The partial derivate of $\rho_a^S$ is

$$\frac{\partial \rho_a^S}{\partial \rho_j} = \frac{1}{2}(\frac{\partial \rho_a^{TM}}{\partial \rho_j} + \frac{\partial \rho_a^{TE}}{\partial \rho_j}), \tag{C.10}$$

$\rho_j$ is the resistivity of the *j–th* block in the model. We also know that

$$\frac{1}{\rho_a^S}\frac{\partial \rho_a^S}{\partial \rho_j} = \frac{1}{|\rho_a^S|}\frac{\partial |\rho_a^S|}{\partial \rho_j} + i\frac{\partial \phi^S}{\partial \rho_j}. \tag{C.11}$$

Using Eqs. (C10) and (C11), we have

$$\frac{1}{|\rho_a^S|}\frac{\partial |\rho_a^S|}{\partial \rho_j} = \frac{1}{2}\mathrm{Re}(\frac{1}{\rho_a^S}\frac{\partial \rho_a^{TM}}{\partial \rho r_j} + \frac{1}{\rho_a^S}\frac{\partial \rho_a^{TE}}{\partial \rho_j}). \tag{C.12}$$

Using a relation similar to Eq. (C11) for $\rho_a^{TM}$ and $\rho_a^{TE}$,

$$\frac{1}{|\rho_a^S|}\frac{\partial |\rho_a^S|}{\partial \rho_j} = \frac{1}{2}\mathrm{Re}\{\frac{\rho_a^{TM}}{\rho_a^S}(\frac{1}{|\rho_a^{TM}|}\frac{\partial |\rho_a^{TM}|}{\partial \rho_j} + i\frac{\partial \phi^{TM}}{\partial \rho_j}) + \frac{\rho_a^{TE}}{\rho_a^S}(\frac{1}{|\rho_a^{TE}|}\frac{\partial |\rho_a^{TE}|}{\partial \rho_j} + i\frac{\partial \phi^{TE}}{\partial \rho_j})\}, \tag{C.13}$$

in terms of apparent conductivities this is:

$$\frac{\partial |\sigma_a^S|}{\partial \sigma_j} = \frac{1}{2}\mathrm{Re}\{\frac{\rho_a^{TM}}{|\rho_a^S||\rho_a^S|}(|\rho_a^{TM}|\frac{\partial |\sigma_a^{TM}|}{\partial \sigma_j} - i\frac{\partial \phi^{TM}}{\partial \sigma_j}) + \frac{\rho_a^{TE}}{|\rho_a^S||\rho_a^S|}(|\rho_a^{TE}|\frac{\partial |\sigma_a^{TE}|}{\partial \sigma_j} - i\frac{\partial \phi^{TE}}{\partial \sigma_j})\}. \tag{C.14}$$

The general expression for the elements of matrix **A** is

$$\frac{1}{2}\mathrm{Re}\{\frac{|\rho_a^{TM}|\rho_a^{TM}}{|\rho_a^S|\rho_a^S}I_{TM} + \frac{|\rho_a^{TE}|\rho_a^{TE}}{|\rho_a^S|\rho_a^S}I_{TE}\}. \tag{C.15}$$

All quantities are obtained directly from the data.

### *Parallel impedance derivative*

For the parallel data, it is better to deal with apparent conductivities

$$\sigma_a^P = \frac{1}{2}(\sigma_a^{TM} + \sigma_a^{TE}). \tag{C.16}$$

The partial derivative with respect to $\sigma_j$ is

$$\frac{\partial \sigma_a^P}{\partial \sigma_j} = \frac{1}{2}(\frac{\partial \sigma_a^{TM}}{\partial \sigma_j} + \frac{\partial \sigma_a^{TE}}{\partial \sigma_j}). \tag{C.17}$$

Writing parallel apparent conductivity as

$$\sigma_a^P = |\sigma_a^P| e^{-i\phi^P}, \tag{C.18}$$

then

$$\frac{1}{\sigma_a^P}\frac{\partial \sigma_a^P}{\partial \sigma_j} = \frac{1}{|\sigma_a^P|}\frac{\partial |\sigma_a^P|}{\partial \sigma_j} - i\frac{\partial \phi^P}{\partial \sigma_j}. \tag{C.19}$$

Using Eq. (C17)

$$\frac{1}{|\sigma_a^P|}\frac{\partial |\sigma_a^P|}{\partial \sigma_j} = \frac{1}{2}\mathrm{Re}(\frac{1}{\sigma_a^P}\frac{\partial \sigma_a^{TM}}{\partial \sigma_j} + \frac{1}{\sigma_a^P}\frac{\partial \sigma_a^{TE}}{\partial \sigma_j}). \tag{C.20}$$

Using a relation similar to Eq. (C11) but for $\sigma_a^{TM}$ and $\sigma_a^{TE}$, we have

$$\frac{\partial |\sigma_a^P|}{\partial \sigma_j} = \frac{1}{2}\mathrm{Re}\{|\sigma_a^{TM}| e^{i(\phi^P - \phi^{TM})}(\frac{1}{|\sigma_a^{TM}|}\frac{\partial |\sigma_a^{TM}|}{\partial \sigma_j} - i\frac{\partial \phi^{TM}}{\partial \sigma_j}) + |\sigma_a^{TE}| e^{i(\phi^P - \phi^{TE})}(\frac{1}{|\sigma_a^{TE}|}\frac{\partial |\sigma_a^{TE}|}{\partial \sigma_j} - i\frac{\partial \phi^{TE}}{\partial \sigma_j})\}. \tag{C.21}$$

The general expression for the elements of matrix **A** is

$$\frac{1}{2}\mathrm{Re}\{e^{i(\phi^P - \phi^{TM})}I_{TM} + e^{i(\phi^P - \phi^{TE})}I_{TE}\}. \tag{C.22}$$

Again, all quantities are obtained directly from the data.

## 4 Generalized Model in a Hopfield Artificial Neural Network

It is necessary to define models with more realistic conductivity values (not only 0's and 1's). Therefore, a general model whose states are formed by an ordered set of 0's and 1's is defined to represent a finite precision real number. We will refer to this model as the general sequence model. The general sequence model $\{\sigma_i^g\}_1^N$ has a typical element:

$$\sigma_i^g = \sum_{j=-D}^{U} 2^j B_{ij}^{(t)} - 2^U B, i = 1,2,...,N, \quad \text{(D.1)}$$

where $B_{ij}$ = 0 or 1, $D$ and $U$ are numbers which depend on the model precision and amplitude, respectively, and $B$ numerically equal to unity carries the dimensions of $B_{ij}$. Equation (D1) may be viewed as a binary representation of $\{\sigma_i^g\}_1^N$ with $D$+$U$+1 bits (e.g., Zhang and Paulson, 1997). Hence, for the general sequence model we have

$$C = -\frac{1}{2}\sum_{i=1}^{N}\sum_{m=-D}^{U}\sum_{j=1}^{N}\sum_{n=-D}^{U}[-\sum_{k=1}^{M} 2^{(m+n)} A_{ki}A_{kj}]B_{im}^{(t)}B_{jn}^{(t)}$$

$$- \sum_{i=1}^{N}\sum_{m=-D}^{U}[-\frac{1}{2}\sum_{k=1}^{M}(2^m A_{ki})^2 B_{im}^{(t)} + \sum_{k=1}^{M}(2^m A_{ki})s_k^a + \sum_{k=1}^{M}\sum_{j=1}^{N}(2^{(m)+U})A_{ki}A_{kj})B]B_{im}^{(t)}$$

$$+ (a\text{-}term\text{-}independent\text{-}of\text{-}the\text{-}model). \quad \text{(D.2)}$$

Once again, comparison of (D2) and (12) shows that $C$ and $E$ have the same form except for the model-independent term, provided that

$$V_{im} = B_{im}, \quad \text{(D.3)}$$

$$T_{imjn} = [-\sum_{k=1}^{M} 2^{m+n} A_{ki}A_{kj}], with T_{imjn} = 0, for (i,m) = (j,n), \quad \text{(D.4)}$$

and

$$I_{im} = -\frac{1}{2}\sum_{k=1}^{M}(2^m A_{ki})^2 B_{im}^{(t)} + \sum_{k=1}^{M}(2^m A_{ki})\sigma_k^a + \sum_{k=1}^{M}\sum_{j=1}^{N}(2^{(m+U)} A_{ki}A_{kj})B. \quad \text{(D.5)}$$

This way the state of the $B_{im}^{(t+1)}$ neuron after dynamics actualization will be:

$$B_{im}^{(t+1)} = \begin{cases} 1 \ \ if \ \ \sum_{j=1}^{N}\sum_{n=-D}^{U} T_{imjn}B_{jn}^{(t)} + I_{im} > 0 \\ 0 \ \ if \ \ \sum_{j=1}^{N}\sum_{n=-D}^{U} T_{imjn}B_{jn}^{(t)} + I_{im} \le 0. \end{cases} \quad \text{(D.6)}$$

The number of neurons in the network is $N(D+U+1)$, where $D$ and $U$ are large enough to guarantee the amplitude and precision of the model. It should be noted that in order to implement the algorithm on a computer, several optimizations can be made in order to improve both the CPU computation time and memory resources. The program that we used to simulate the RHANN was written in C computer language, in which 32 states of every neuron, namely 0's and 1's, can be stored in a 32-bit wide variable (*unsigned long int value*). Power of 2 expressions such as $2^{(m+n)}$ can be computed and stored in memory as $power2[m+n]$, we also note that $T_{imjn} = [-\sum_{k=1}^{M} 2^{m+n} A_{ki}A_{kj}]$, the values of the products $matk[i][j] = \sum_{k=1}^{M} A_{ki}A_{kj}$ can be calculated and stored in a bi-dimensional array, in order to be used later in the inner loops of the dynamics. This way, we obtain the term $\sum_{i=1}^{N}\sum_{n=-D}^{U} T_{imjn}B_{jn}^{(t)} + I_{im}$ in equation (D6) by including equation (D4). We can state the term as:

$$sum0[i][m] = -\sum_{n=-D}^{U} power2[m+n] * \sum_{j=1}^{N} matk[i][j]B_{jm}^{(t)} \quad \text{(D.7)}$$

Similarly, in equation (D6), for $I_{im}$ the three products within can also be computationally optimized, this way we will define the values $sum1[i][m]$, $sum2[i][m]$ *and* $sum3[i][m]$ as follows:

$$sum1[i][m] = -\frac{1}{2} power2[2*m] * \sum_{k=1}^{M} (A_{ki})^2 B_{im}^{(t)}, \quad \text{(D.8)}$$

$$sum2[i][m] = power2[m] * \sum_{k=1}^{M} (A_{ki})\sigma_k^a, \quad \text{(D.9)}$$

$$sum3[i][m] = power2[m+U] * \sum_{j=1}^{N} matk[i][j], \quad \text{(D.10)}$$

therefore, the dynamics of the state of each neuron $B_{im}^{(t+1)}$ will be updated according to:

$$B_{im}^{(t+1)} = \begin{cases} 1 \ \ if \ \ sum0[i][m] + sum1[i][m] + sum2[i][m] + sum3[i][m] > 0 \\ 0 \ \ if \ \ sum0[i][m] + sum1[i][m] + sum2[i][m] + sum3[i][m] \le 0. \end{cases} \quad \text{(D.11)}$$

Furthermore, it should be noted that the simple binary natural representation of the problem makes it suitable to be solved by a device which is capable of accumulating sums of partial products (vector/matrix computation). Such devices are currently available in the form of an electronic circuit known as a Digital Signal Processor (DSP) or the more versatile Field Programmable Gate Array (which might have embedded DSPs included). Such circuits are capable of fast multiplication-accumulation processing. If such a custom digital computer could be realized, it could reduce the computation times achieved by current traditional CPU based computers.